J. Fluid Mech. (1998), *vol.* 360, *pp.* 73–84 Printed in the United Kingdom

Some aerodynamic aspects of coin-like cylinders

By M. M. ZDRAVKOVICH[1], A. J. FLAHERTY[2], M. G. PAHLE[2] AND I. A. SKELHORNE[2]

[1] Telford Institute, University of Salford, Salford M4 4WT, UK

[2] Department of Aeronautical, Mechanical, and Manufacturing Engineering, University of Salford, Salford M5 4WT, UK

(Received 29 July 1996 and in revised form 1 December 1997)

The aspect ratio of short coin-like cylinders is defined as L/D, where L is the length and D is the diameter of the cylinder. Force and pressure measurements are extended down to $L/D = 0.025$. The force measurements indicate an unexpected increase in drag coefficient with decreasing aspect ratio. The basic equation used to define the drag coefficient is inapplicable for very low aspect ratio and the projected area should be replaced by the side area. Surface flow visualization tests in a wind tunnel reveal the variation in both shape and size of separation bubbles, which form on the flat sides of the model. A crescent-shaped area is observed between the primary and secondary separation, followed by an unsteady re-attachment region. A strong hysteresis effect is observed in the development of the separation bubbles. The separation bubbles can be suppressed by rounding the sharp edges of the model, with considerable reduction in the drag coefficient. Finally, a flow topology is suggested consisting of two horseshoe vortices attached onto the flat sides and detached in a streamwise direction, thus forming two counter-rotating vortex pairs.

1. Introduction

Wieselsberger (1922) was among the first to report drag measurements on a circular cylinder with two free ends having the aspect ratio $L/D = 5$, where L is the length and D the diameter of the cylinder. He covered an enormous range of Reynolds numbers from 400 to 800×10^3. The drag coefficient, C_D, curve varied with the Reynolds number in a similar manner to that for the nominally two-dimensional cylinder, $L/D = \infty$, but it was displaced towards lower C_D values. For example, the plateau for the subcritical regime occurred for $C_D = 0.78$ instead of $C_D = 1.2$ for $L/D = \infty$. The drastic fall in C_D values in the critical regime $Re > 4 \times 10^5$ took place at the same Reynolds number and towards the same value of $C_D = 0.3$ as for $L/D = \infty$. Subsequently, Wieselsberger (see Muttray 1932) examined the effects of aspect ratio on the drag coefficient for $Re = 8.8 \times 10^4$. Figure 1 shows a compilation of drag coefficient values in terms of both L/D and D/L down to $L/D = 1$.

Zdravkovich *et al.* (1989) repeated Wieselsberger's tests and also examined the effect of hemispherical ends on the drag coefficient. Figure 1 shows a considerable reduction in drag coefficient for the latter, which is an indication that flat sides contribute to the overall drag. Note that as the aspect ratio decreases, the cylindrical part of the cylinder shrinks and for $L/D = 1$ the 'cylinder' with two hemispherical ends becomes a sphere. However, when the cylinder has two flat sides it is possible to reduce the aspect ratio down to $L/D \to 0$, but the drag cannot tend to zero because of skin friction on both sides. The aspect ratios in the range $0 < L/D < 1$ will be examined in some detail in

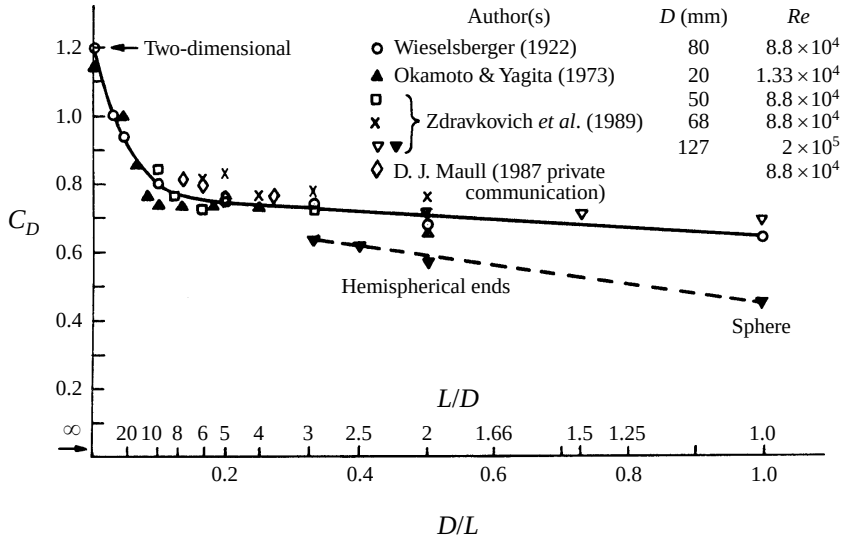

FIGURE 1. Drag coefficient compilation in terms of aspect ratio (Zdravkovich *et al.* 1989).

the present paper. The effect of free ends becomes dominant in that range and the Reynolds number still determines the boundary layer characteristics and the skin friction drag.

The practical applications of coin-like cylinders are numerous, such as aircraft, car and bicycle wheels, cylindrical objects carried by a tornado as deadly projectiles, submerged remotely operated vehicles (ROV), frisbee (with added rotation) discs like AWAC radar, etc. In most of these applications, the main interest is the drag force and its reduction. There is also a fundamental interest in such highly complex three-dimensional flows. They exhibit three kinds of separation: (i) salient primary separation from sharp edges; (ii) secondary separation of the reversed flow along the flat sides; (iii) separation from the circumference of the cylinder due to the adverse pressure gradient. There may be a re-attachment of the flow onto the flat sides and formation of separation bubbles in addition to the main unsteady separation region – the near wake. The aim of the tests described in the present study was to gain some insight into the topology and interaction of these flow structures.

2. Experimental arrangement

2.1. *Wind tunnels*

Tests have been carried out in two wind tunnels. The first was of a closed-circuit type having a test section 0.91 m high, 1.24 m wide, and 1.80 m long. The speed could be varied up to 40 m s^{-1} and the local free-stream turbulence was around 1 %. Above the test section there was a six-component strain-gauge aerodynamic balance which was used to measure drag force only.

The second wind tunnel was of an open-circuit type having a test section of 0.46 m × 0.46 m in cross-section and 1.38 m long. The speed could be varied up to 46 m s^{-1} and free-stream turbulence intensity was approximately 1 %. This wind tunnel was used for all pressure distribution measurements and surface flow visualization.

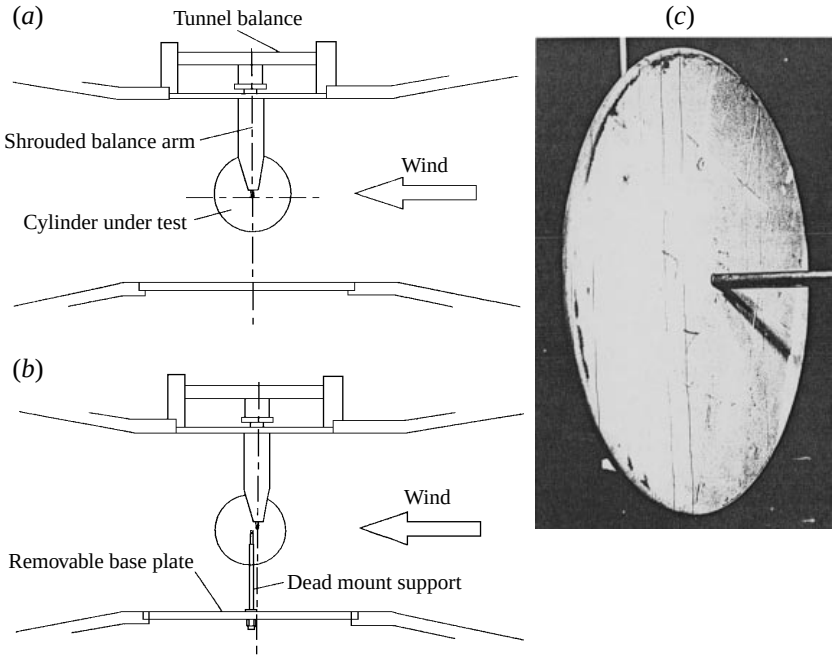

FIGURE 2. Model (*a*) suspended on balance, (*b*) attached to floor of test section, (*c*) front view.

2.2. *Models*

Different models were made for the force and pressure measurements. Four cylinders 30 cm diameter were used for the former, having aspect ratios, $L/D = 0.07$, 0.13, 0.25 and 0.5. By combining these models it was possible to have $L/D = 0.37$, 0.63, 0.75 and 0.89. The flat free ends on all models were made with sharp edges. Two additional models of 60 cm diameter were made to $L/D = 0.025$ and 0.050, having either sharp or rounded edges on both sides. The attachment of the models to the aerodynamic balance above the test section is illustrated in figures 2(*a*) and 2(*c*). The measured drag force consisted of two components produced by the model and its support. The support drag force was measured by attaching the model to the floor of the test section, as shown in figure 2(*b*). The maximum blockage was 4.3%.

The basic model for pressure measurements and surface flow visualization was 8.9 cm in diameter, 0.9 cm wide, giving $L/D = 0.11$, as shown in figure 3. It was provided with eight pressure tappings around the circumference at 0°, 30°, 60°, 75°, 90°, 105°, 120° and 135°. There was also six pressure tappings on one flat side at a 2.4 cm radius at 0°, 37.5°, 67.5°, 112.5° and 180°, plus one at 1.6 cm radius 0°. Two central pressure tappings on both flat sides ($R = 0$) were provided for the alignment of the model to a zero yaw angle. The aspect ratio was varied by adding cylindrical inserts 8.9 cm in diameter and having $L/D = 0.06$, 0.13, 0.25, 0.31 and 0.40. Maximum blockage ratio for $L/D = 0.89$ with supports was 3.5%. The inserts could be attached either symmetrically when the pressure distribution was measured along the equatorial axis or asymmetrically when the pressure distribution was measured at $Z/D = 0.055$ from the flat side.

The model was attached to a sting mount in a vertical position, as seen in figure 3. The L-shaped sting was fastened to an adjustable turntable in the test section. The sting mount, attached to the rear of the model, covered the arc from 165° to 195° of the

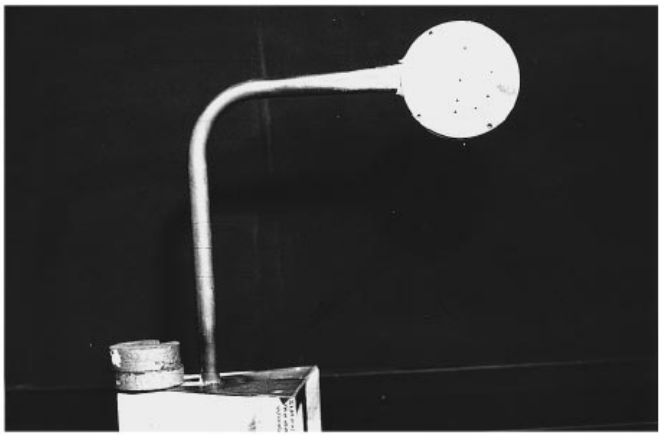

FIGURE 3. Model mounted on sting ($D = 8.9$ cm, flow from right to left).

model. It had an oval shape 2.0 cm $\times$ 0.6 cm, slightly narrower than the 0.9 cm width of the basic model ($L/D = 0.11$). The rest of the sting was made of a hollow steel tube 1.5 cm in diameter which accommodated sixteen plastic tubes attached to the pressure tappings around and on the sides of the model. It was originally envisaged that, although the sting was completely shielded by the model, it might affect the separation from the circumference and the base pressure in the near wake. This was checked and found not to be the case.

2.3. *Surface flow visualization*

An extensive surface flow visualization was carried out on all models. A white talcum powder–paraffin mix was applied with a brush to acetate sheets glued onto the model surface. During the run, the paraffin evaporated and a distinct surface pattern revealed a time-average secondary separation and re-attachment region on the flat sides and separation lines on the circumference of the model.

3. Experimental results

3.1. *Drag measurements*

The original aim of the drag measurements was to confirm an expected further decrease in drag coefficient for aspect ratios below 1. The decrease in drag coefficient was expected because the 'bluffness' of the coin-like cylinder decreased and eventually, when $L/D \rightarrow 0$, only the friction drag was present along the flat sides of an extremely thin disc.

Several test runs were carried out using various models and the drag coefficient, in terms of L/D, is plotted in figure 4. The unexpected increase in drag coefficient with the decreasing aspect ratio is evident.

The scatter of experimental points obtained in the same run did not exceed $\pm 4\,\%$. However, there was always a systematic departure of experimental points obtained in different runs up to $\pm 8\,\%$, thought to be due to a slight misalignment of the models. The same effect was also noted and quantified for bicycle wheels, Zdravkovich (1992). The proportion of the support drag relative to the total drag was less than 10 % and was dependent on the aspect ratio.

Another point worth noting was that the tests were carried out in the critical regime, $2 \times 10^5 < Re < 6 \times 10^5$, where a drastic drop in C_D was found at $Re = 4 \times 10^5$ for

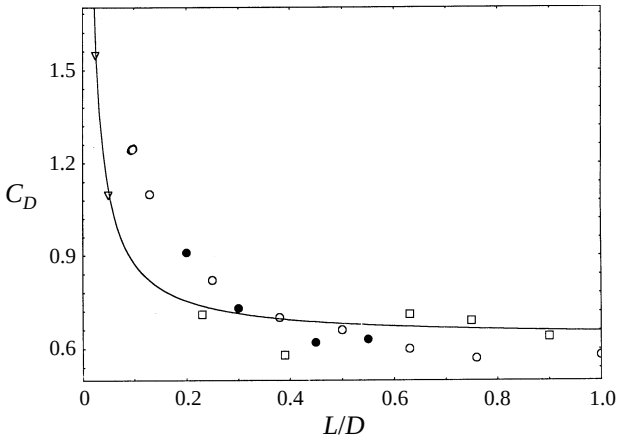

FIGURE 4. Measured drag coefficient in terms of aspect ratio: □, early tests; ○, second tests; ●, repeated tests; ▽, 60 cm disc; best fit curve $C_D = 0.24/L/D + 0.633$.

L/D	Rounded edge	Sharp edge	C_D reduction
0.05	0.73	1.10	33.6%
0.03	1.18	1.51	17.7%

TABLE 1. Drag coefficient for sharp and round edges

$L/D = 5$ by Wieselsberger (1922). A similar Reynolds number effect has not been found for the coin-like cylinders up to $Re = 6 \times 10^5$. The 60 cm diameter models were provided with rounded edges (like the bicycle wheel) and the drag was measured again. The drag coefficient is given in table 1.

These simple tests demonstrated that separation bubbles that formed around sharp edges did contribute to the overall drag. The re-attachment of separated shear layers might have an additional effect because it caused a considerable adverse pressure recovery along the surface. This is to be discussed in more detail in the following subsections.

The increase in drag coefficient for coin-like cylinders may be circumvented by replacing the projected area, LD, by the side area, $D^2\pi/4$, as the reference area:

$$C_{DS} = C_D \frac{L}{D} \frac{4}{\pi}, \tag{1}$$

where C_{DS} is the new drag coefficient and C_D is the old conventional drag coefficient. Figure 5 shows the variation of C_{DS} in terms of the aspect ratio of the model: it appears that the increase is only apparent due to the inappropriate formulation of the reference area.

3.2. *Pressure distribution around a circumference*

The tests were carried out in the second wind tunnel using 8.9 cm diameter models mounted on the sting, figure 3. It had been established that the pressure distribution did not depend on Reynolds number and tests were restricted to $Re = 2.4 \times 10^5$. The aspect ratio was varied by adding cylindrical sections either symmetrically on both sides of the basic model or asymmetrically on one side only. These two arrangements allowed two pressure distributions to be measured in separate runs along the middle

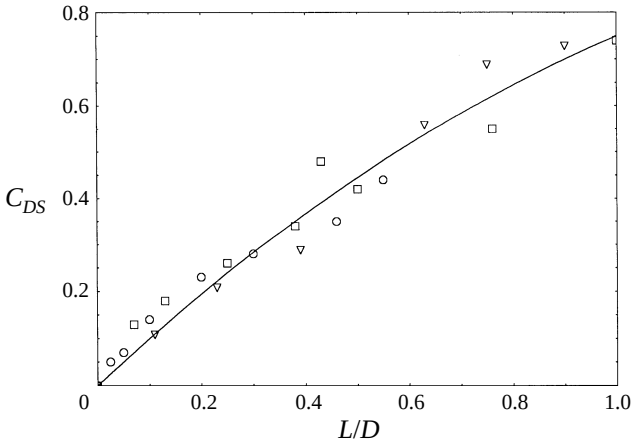

FIGURE 5. Drag coefficient based on side area in terms of aspect ratio (all tests).

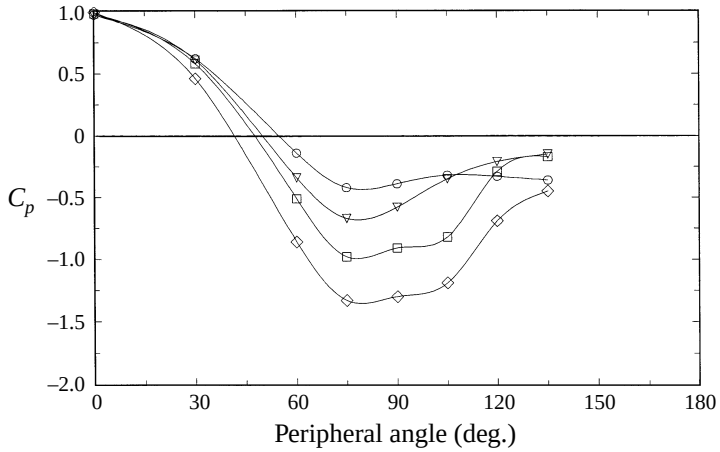

FIGURE 6. Pressure coefficient distribution around circumference at mid-span for ○, $L/D = 0.11$; ▽, 0.23; □, 0.39, ◇, 0.63.

and near the flat side of the model, respectively. Note that for the basic model, $L/D = 0.11$, only the pressure distribution at the middle plane could be measured.

Figure 6 shows a typical mid-span pressure distribution for various aspect ratios. The highest $-C_{pmin}$ is found for $L/D = 0.11$ and the lowest $-C_{pmin}$ for $L/D = 0.63$. The variation in pressure distribution for the same L/D at the side and the mid-span is shown in figure 7, where the distribution for $L/D = 0.11$ is added for comparison. There are three unexpected features. (i) The positive part of the windward pressure distribution curve is spread towards higher circumferential angles in comparison with the nominally two-dimensional cylinder. For example, $C_p = 0$ is at $\theta = 55°$ for $L/D = 0.11$ but $\theta = 35°$ for $L/D \to \infty$. (ii) The base pressure coefficient is only -0.36 compared with -1.4 for the nominally two-dimensional cylinder. The strong three-dimensional flow towards the wake of the model considerably reduces the negative base pressure. (iii) A pressure recovery is seen for $\theta > 100°$. It may have been caused by the sting of $\theta > 165°$, but this is not the case and will be discussed in the next section.

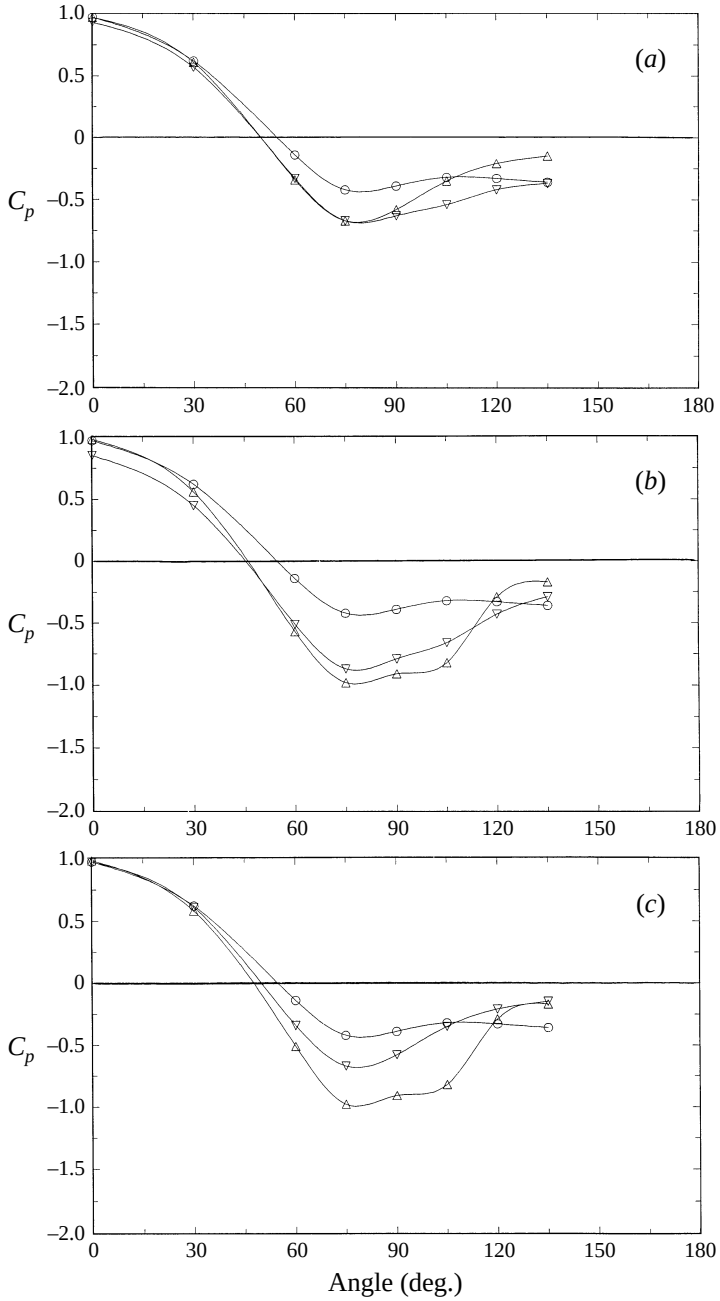

FIGURE 7. Pressure distribution versus circumferential angle: for (*a*) $L/D = 0.23$, (*b*) $L/D = 0.39$, (*c*) $L/D = 0.75$. △, mid-span; ▽, side. For comparison: ○, $L/D = 11$.

3.3. *Surface flow visualization*

Flow around coin-like cylinders is dominated by the salient separation from the sharp edges along the circumference on both sides. The separated shear layers may re-attach onto the flat sides and the region between the primary salient separation from the sharp edge and re-attachment forms the separation bubble, see the review by Kiya & Sasaki (1983). The reversed flow along the surface underneath the separation bubble

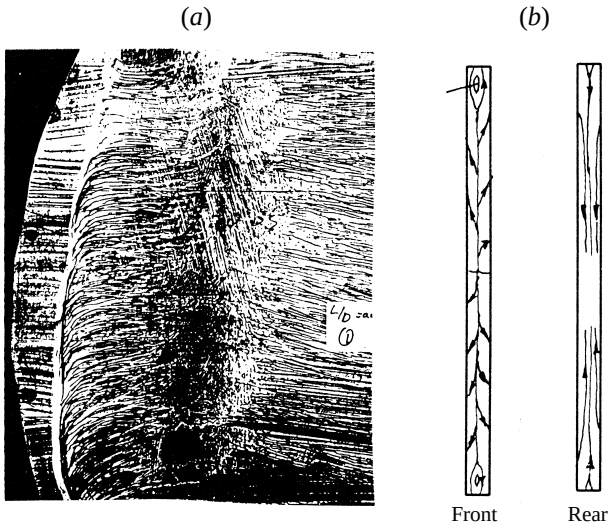

FIGURE 8. (*a*) Surface pattern on flat side, (*b*) developed pattern on cylindrical section (Sketch), for $L/D = 0.05$ at $Re = 5.9 \times 60$ cm model).

eventually detaches from the surface as the secondary separation. Surface flow visualization shows distinctly an almost steady secondary separation line and, less distinctly, the unsteady re-attachment region.

Figure 8 shows the surface pattern for $L/D = 0.05$ at $Re = 5.4 \times 10^5$ on the large 60 cm diameter model in wind tunnel 1. The flat side of the model is covered with six A4 acetate sheets, but only the pattern on the central windward sheet is reproduced in figure 8(*a*). There are three regions displayed in the surface pattern. (i) The stagnant area between the primary and secondary separations forms a crescent shape. (ii) The re-attachment region appears straight and vertical in figures 8(*a*) and 9(*b*). (iii) The flow remains attached to the surface beyond the re-attachment region. This area extends up to the trailing edge of the flat side (not covered in figure 8*a*).

Figure 8(*b*) shows the developed surface pattern around the perimeter of the cylindrical section for the $L/D = 0.05$. There are three features: (i) The three-dimensional flow is characterized by the lateral outflow components from the axis of symmetry towards the two sides. (ii) The separation line degenerates to a separation 'islet'. Two such 'islets' are seen in figure 8(*b*) at around $\theta = 90°$. Note that this model is not supported by the sting and this flow feature cannot be attributed to the sting interference. (iii) The reason for the disappearance of separation lines can be found in the surface pattern along the leeward side. The three-dimensional flow is characterized by surface lines directed from the sides toward the model axis of symmetry. This inflow gradually stops at around $\theta = 160°$ and is produced by the base pressure difference between the middle and side planes.

Figure 9(*a*) shows surface patterns on the flat side of the $L/D = 0.11$ model at $Re = 2.14 \times 10^5$. The size of the model (30 cm diameter) allows full coverage with a single A4 acetate sheet. The secondary separation forms a crescent-like area, as in figure 8(*a*). The re-attachment may be inferred from the spanwise surface pattern covering a vertical strip and being a time-average imprint of the unsteady surface flow. The positions of the secondary separation and re-attachment along the equatorial axis of the flat side are at $X/D = 0.11$ and 0.31, respectively. Figure 9(*b*) shows a considerable downstream displacement of the re-attachment for $L/D = 0.39$ in comparison with

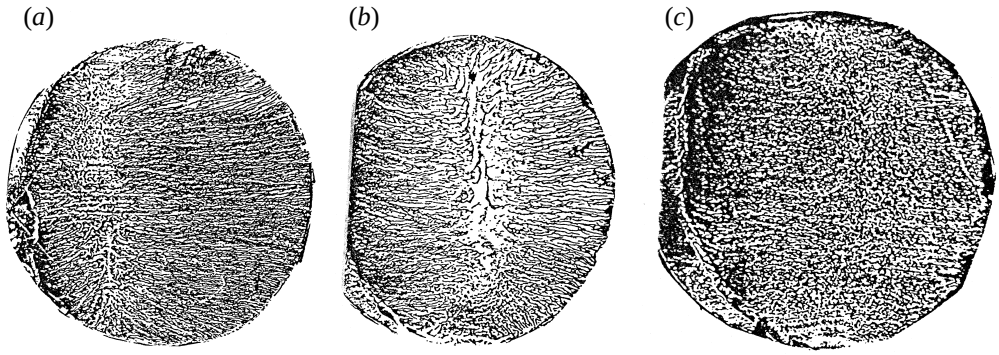

FIGURE 9. Surface pattern on the flat side at $Re = 2.14 \times 10^5$ (8.9 cm model) for (*a*) $L/D = 0.11$, (*b*) 0.39, (*c*) 0.75.

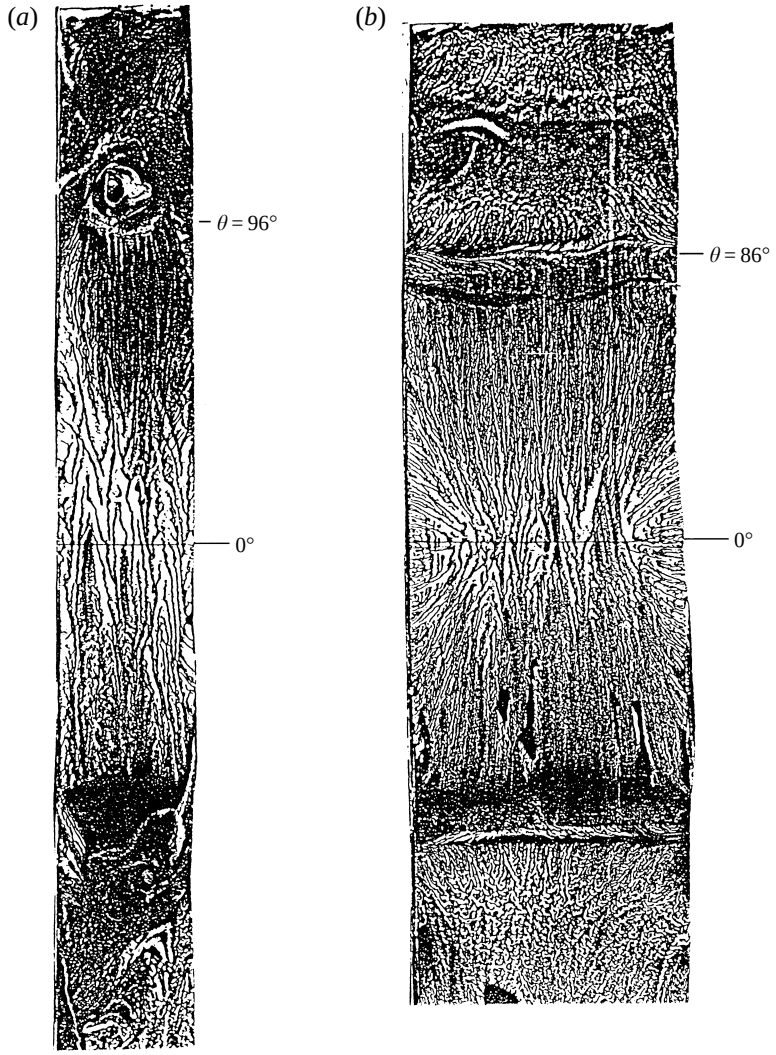

FIGURE 10. Developed surface pattern on the cylindrical sections (8.9 cm diameter), (*a*) $L/D = 0.39$, (*b*) $L/D = 0.75$.

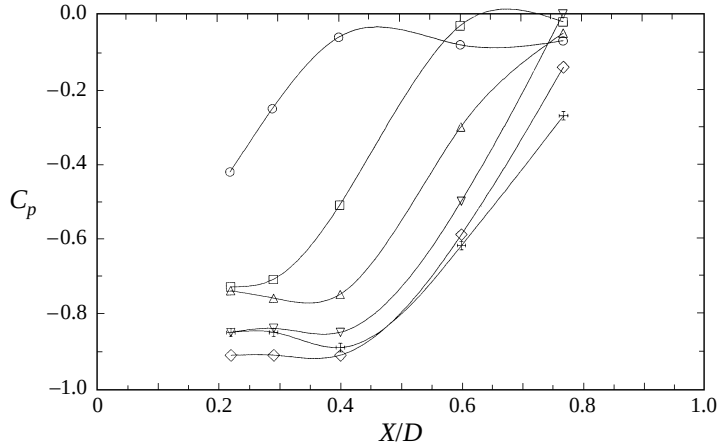

FIGURE 11. Pressure distribution along flat side at $Re = 2.1 \times 10^5$ for ○, $L/D = 0.11$; □, 0.23; △, 0.39; ▽, 0.63; ◇, 0.75; +, 0.90.

figure 9(*a*). Finally, figure 9(*c*) shows the surface pattern for $L/D = 0.75$ and it seems that the separated shear layer does not re-attach onto the flat side.

Figures 10(*a*) and 10(*b*) show the surface pattern along the perimeter of the cylindrical sections of two models, $L/D = 0.39$ and 0.75, respectively. (Note that both acetate strips extended only up to $\pm 140°$). The separation 'islets' are seen in figure 10(*a*) for $L/D = 0.39$ at $\theta \pm 96°$. However, they are replaced by separation lines at $\theta = \pm 86°$ in figure 10(*b*).

Initially, the separation 'islets' were assumed to be due to sting interference. The surface visualization was performed on $L/D = 0.39$ model, mounted on the sting support and on the central transverse rod. Identical separation 'islets' were found in the same location in both cases. This confirmed that the separation 'islets' were an intrinsic feature of the low-aspect-ratio cylinders and they were caused by the disruption of separation lines by the flow along the edges.

3.4. *Side pressure distribution*

The qualitative features of the mean surface flow revealed by the flow visualization were confirmed by the local static pressure measured along one flat side of the models. The area under the separation bubble was associated with low pressure, the re-attachment region caused the adverse pressure recovery and the re-attached flow was characterized by the closeness to the free-stream pressure, i.e. $C_p \to 0$, see the review by Roshko (1993).

Figure 11 shows the pressure coefficient distribution measured on the flat side of the models for $0.11 < L/D < 0.89$ at $Re = 2.14 \times 10^5$. The pressure tappings were arranged along a semicircle of 2.4 cm radius at $\theta = 0°$, 37.5°, 67°, 112.5° and 180°. (Note that only the first and last tapping lie on the equatorial axis.) The lowest-aspect-ratio model, $L/D = 0.11$, shows the earliest pressure recovery due to the shortest separation bubble. There is a considerable displacement of the pressure recovery for $L/D = 0.23$ and it proceeds at a slower rate as the aspect ratio increases. For example, the pressure distributions for $L/D = 0.74$ and 0.89 are barely different. The free-stream pressure ($C_p = 0$) is not reached and this may indicate that the re-attachment occurs beyond $X/D = 0.76$, the last available pressure tapping.

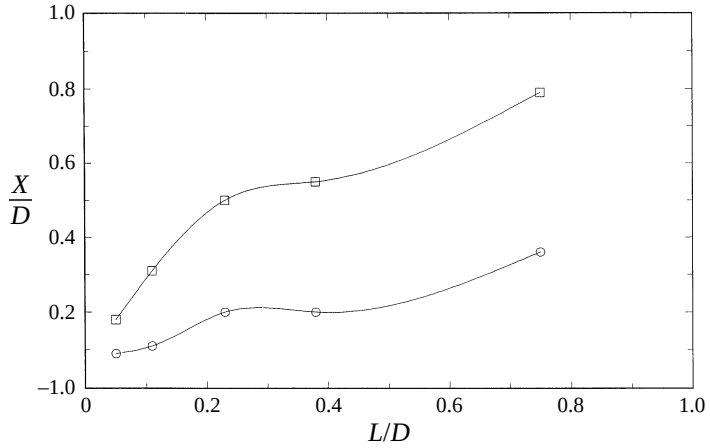

FIGURE 12. Relative positions of re-attachment and secondary separation in terms of aspect ratio: ○, secondary separation; □, re-attachment.

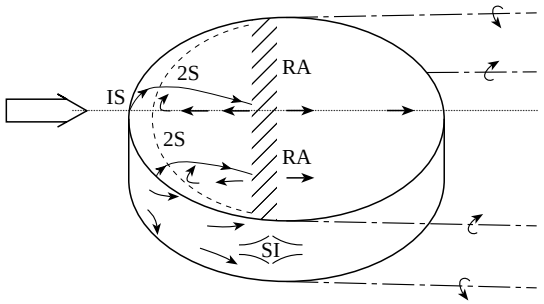

FIGURE 13. Tentative sketch of flow topology: IS – primary separation; 2S – secondary separation; SI – separation islet; RA ..., re-attachment; ---, separation bubble; –·–, streamwise vortex filaments.

3.5. *Separation bubbles*

The appearance of the separation bubbles on the flat sides of coin-like cylinders is caused by the salient separation from the sharp edges and subsequent re-attachment. There is a strong variation in size of the separation bubbles with the aspect ratio. Figure 12 shows the estimated relative position of the re-attachment region (squares) and secondary separation (circles) along the equatorial axis of the model. Note that the length of the separation bubble is designated by the re-attachment curve (top). Despite the semicircular shape of the primary separation line, the re-attachment line appears as an almost straight line. The initial three-dimensional separation produces a two-dimensional re-attachment.

A tentative attempt to specify flow topology is shown in figure 13. Beyond the perimeter of the cylinder, two pairs of streamwise eddies are carried downstream. The geometry of these horseshoe eddies was visualized beyond a stationary frisbee in a wind tunnel by Nakamura & Fukamachi (1991). The position of the separation islet on the cylindrical segment coincides with the eddy pairs.

4. Conclusions

The unexpected increase in drag coefficient for low-aspect-ratio cylinders has prompted the present research. The main findings are as follows:

There is a systematic increase in the conventional drag coefficient (expressed through the projected area L/D) up to 1.5 for $L/D = 0.06$. The apparent increase in the conventional drag coefficient disappears when a new drag coefficient, scaled by the side area as the reference area, is used.

The elimination of the separation bubbles by rounding the edges ($R = \frac{1}{2}L$) produces a considerable reduction in the measured drag coefficient.

The surface flow visualization on two flat sides reveals crescent-shaped areas between primary separation from the sharp edges and secondary separation of the reversed flow underneath the separation bubbles. The re-attachment region appears to be straight and perpendicular to the free stream. The surface flow visualization around the cylindrical section reveals the gradual disappearance of separation lines in the range $0.39 < L/D < 0.75$ and the appearance of separation 'islets' for $L/D < 0.39$. The change in separation is caused by the three-dimensional flow.

A tentative topology of the flow around coin-like cylinders is proposed; it may consist of two horseshoe-shaped vortices attached onto the two flat sides. After their detachment at around $\pm 90°$, the free vortices are coupled into two counter-rotating pairs on the leeside.

The first author would like to give credit for the experimental work carried out as final-year projects by the three co-authors being, at that time, undergraduate students at the University of Salford. We would like to thank Dr E. M. Laws who kindly read and improved the manuscript, and all the referees who made valuable suggestions.

REFERENCES

Kiya, M. & Sasaki, K. 1983 Structure of turbulent separation bubble. *J. Fluid Mech.* **137**, 83–113.

Muttray, H. 1932 The experimental facts of drag without lift (German). In *Handbuch der Experimental-Physik*, vol. 4.2 (ed. L. Schiller) pp. 318–321.

Nakamura, Y. & Fukamachi, N. 1991 Visualisation of the flow past a frisbee. *Fluid Dyn. Res.* **7**, 31–35.

Okamoto, T. & Yagita, M. 1973 The experimental investigation on the flow past a circular cylinder of finite length placed normal to the plane surface in a uniform stream. *Bull. JSME* **16**, 805–814.

Roshko, A. 1993 Free shear layers, base pressure, and bluff body drag. In *Proc Symp. Developments in Fluid Dynamics and Aerospace Engineering*, Bangalore, India, 9–10 December.

Wieselsberger, C. 1922 Further data on the law of liquid and air drag (German). *Phys. Z.* **23**, 219–224.

Zdravkovich, M. M. 1992 Aerodynamics of bicycle wheel and frame. *J. Wind Engng Ind. Aerodyn.* **40**, 55–70.

Zdravkovich, M. M., Brand, V. P., Matthew, G. & Weston, A. 1989 Flow past short circular cylinders with two free ends. *J. Fluid Mech.* **203**, 557–575.